

**Depression of melting point and latent heat of molten salts as inorganic phase change material: size effect and mechanism**

*Shuai Zhang<sup>a</sup>, Yingai Jin<sup>b</sup>, Yuying Yan<sup>a</sup> \**

<sup>a</sup> Faculty of Engineering, University of Nottingham, University Park, Nottingham, UK

<sup>b</sup> State Key Laboratory of Automotive Simulation and Control, Jilin University, Changchun, China

\* Corresponding author, E-mail: [Yuying.Yan@nottingham.ac.uk](mailto:Yuying.Yan@nottingham.ac.uk)

**ABSTRACT**

The depression of melting point and latent heat is a common phenomenon for nanoporous shape-stabilised phase change materials (ss-PCMs), however, the underlying mechanism is not well understood, especially from the microscopic perspective. As PCMs are embedded in nanopores, the depression of thermal properties may be due to the size effect, interaction effect or both. In this paper, the size effect on thermal properties was studied using a molecular dynamics simulation and the underlying mechanism was explored. NaCl was selected as PCM and the size of the nanoparticle is from 2 nm to 9 nm. Bulk molten salt was also simulated to validate the correctness of the simulation results. It is found that atoms in smaller nanoparticles vibrate more intensely so the crystal structure of smaller nanoparticle is easier to be destroyed, leading to a lower melting point. The lower coordination number indicates the more loosely packed structure. Thus, less energy is required to destroy the crystalline lattice and the latent heat is decreased. This paper reveals the underlying mechanism of the depression of melting point and latent heat from the atomic point of view and paves the way for further studying the depression of thermal properties of PCMs embedded in nanopores.

**Keywords:** phase transition, molten salt, melting point, atomic motion, size effect, shape-stabilised phase change material

## 1. Introduction

Using renewable energy is one of the most effective methods to cope with the worldwide energy crisis and environmental pollution [1]. Some energy resources, such as solar energy, have the drawbacks of intermittence and instability, which hampers their efficiency seriously [2]. One of the solutions is to store surplus thermal energy into phase change materials (PCMs) and release it when the energy is needed, which effectively addresses the mismatch between energy supply and demand [3]. However, the thermal energy storage (TES) system using the pure PCM commonly suffers from the leakage problem and the low thermal conductivity [4]. To overcome these drawbacks, the most popular method is to impregnate PCMs into porous materials to fabricate shape-stabilised phase change materials (ss-PCMs) [5].

Melting point and latent heat are critical thermal properties for ss-PCMs because they determine the application scenarios and heat storage capacity. However, the depression of melting point and latent heat is a common phenomenon for nanoporous ss-PCMs. Nomura et al. [6] prepared three octadecane/mesoporous SiO<sub>2</sub> phase change composites and the average pore size was 11.6 nm, 16.2 nm and 50.0 nm respectively. They found that the melting point of the composite decreased with the decreasing pore size. The three composites had almost the same porosity and impregnation ratio but their latent heat decreased as the decline of the pore size. Mitran et al. [7] used lauric acid (LA) as PCM and three mesoporous silica as supports: MCM-41 (2.8 nm), SBA-15 (6.3 nm) and MCF with a pore size range of 10.4 - 14.9 nm and 27 - 34.9 nm. In their report, the melting point of LA/MCF composite (14.4 °C) was much lower than that of the pure LA (42.7 °C). The experimental latent heat of the prepared nanoporous ss-PCM was less than the theoretical value. Later, they prepared nitrate eutectic/mesoporous silica ss-PCMs. The depression of melting point and latent heat was also observed and the non-melting layer theory was used to explain this phenomenon [8]. Liu et al. [9] fabricated a series of adipic acid/silica-based ss-PCMs with the pore size ranging from 3.3 nm to 24.6 nm. The

melting point showed a linear relationship with the inverse pore size. They also found that measured latent heat decreased with the decreasing pore size. Mitran et al. [8]

As PCMs are embedded in nanopores, the depression of melting point and latent heat may be due to the size effect, the interaction effect or both. The size effect on thermal properties has been observed by many researchers, both in experiments and in simulations. Lee et al. [10] prepared Pd nanowires using mesoporous silicate materials as template. In their experiment, the melting point of Pd nanowire with a diameter of 4.6 nm was 300 °C, a depression of more than 1100 °C compared to the bulk melting point (1445 °C). Wang et al. [11] prepared Zn nanowires with different diameters using porous anodic alumina membrane and found that the melting point decreased with the decreasing nanowire size and was curvilinear with the reciprocal of the nanowire diameter. In many times, it is difficult to use experimental methods to measure thermal properties of nanoscale materials due to technical limitations and extreme conditions [12, 13]. Thus, some researchers sought an alternative approach and adopted the molecular dynamics (MD) method. Chen et al. [14] performed an MD simulation with the isotropic PAHAP potential to study the size-dependent melting of C<sub>16</sub>H<sub>10</sub> and C<sub>24</sub>H<sub>12</sub>. They found that the melting point decreased with the decreasing nanocluster diameter and it followed a linear function with the inverse diameter. Loulijat et al. [15] simulated the melting of Cu nanoparticles and found that the melting point of Cu nanoparticles decreases with the decreasing particle size. They also used the Gibbs equation to calculate the melting point:

$$T_m^N = T_m^B \left( 1 - \frac{2}{\rho_s L r} \left( \gamma_s - \gamma_l \left( \frac{\rho_s}{\rho_l} \right)^{2/3} \right) \right) \quad (1)$$

where  $T_m^B$  and  $T_m^N$  are the melting point of bulk material and nanoparticle,  $\gamma_l$  and  $\gamma_s$  are the surface tension,  $\rho_s$  and  $\rho_l$  are the density,  $L$  is the latent heat and  $r$  is the nanoparticle radius. This theoretical equation is based on equating the Gibbs free energies of solid and liquid nanoparticles. Zhang and He [16] investigated the melting point of Cu nanowire. Their

simulation results indicate that the melting point decreased from 1087 °C to 207 °C when the diameter of Cu nanowire reduced from 6 nm to 2 nm.

Although some work has been done to investigate the size effect on melting point and latent heat, the underlying mechanism is not well understood, especially from the microscopic perspective. Thus, this paper aims to reveal the mechanism of the size effect on thermal properties from the atomic point of view. NaCl was selected as PCM and a molecular dynamics simulation was performed. The size of NaCl nanoparticles is from 2 nm to 9 nm. The bulk molten salt was also simulated to validate the correctness of the simulation results. This paper provides microscopic insights into the depression of melting point and latent heat and paves the way for further studying the depression of thermal properties of PCMs embedded in nanopores.

## 2. Theory and methods

### 2.1. Force field

The Born-Mayer-Huggins pair potential has been proved to properly reproduce the pairwise interaction between ions in molten chloride salts [17]. Thus the Born-Mayer-Huggins potential is adopted in this study:

$$E_{ij} = A_{ij} e^{(\sigma_{ij} - r_{ij})/\rho} - \frac{C_{ij}}{r_{ij}^6} - \frac{D_{ij}}{r_{ij}^8} \quad (2)$$

where  $r_{ij}$  is the distance between two ions;  $A_{ij}$ ,  $\sigma_{ij}$ ,  $C_{ij}$  and  $D_{ij}$  are Born-Mayer-Huggins potential parameters;  $\rho$  is the ionic-pair dependent length parameter, taken as 0.317 Å for NaCl [18]. The first term in Equation (2) stands for Born-Huggins short distance repulsive force; the second term and the third term denote the van der Waals interactions [19, 20].

Coulombic interaction is computed as:

$$E_{coul} = \frac{q_i q_j}{r_{ij}} \quad (3)$$

where  $q_i$  and  $q_j$  are the charge of ion  $i$  and ion  $j$ .

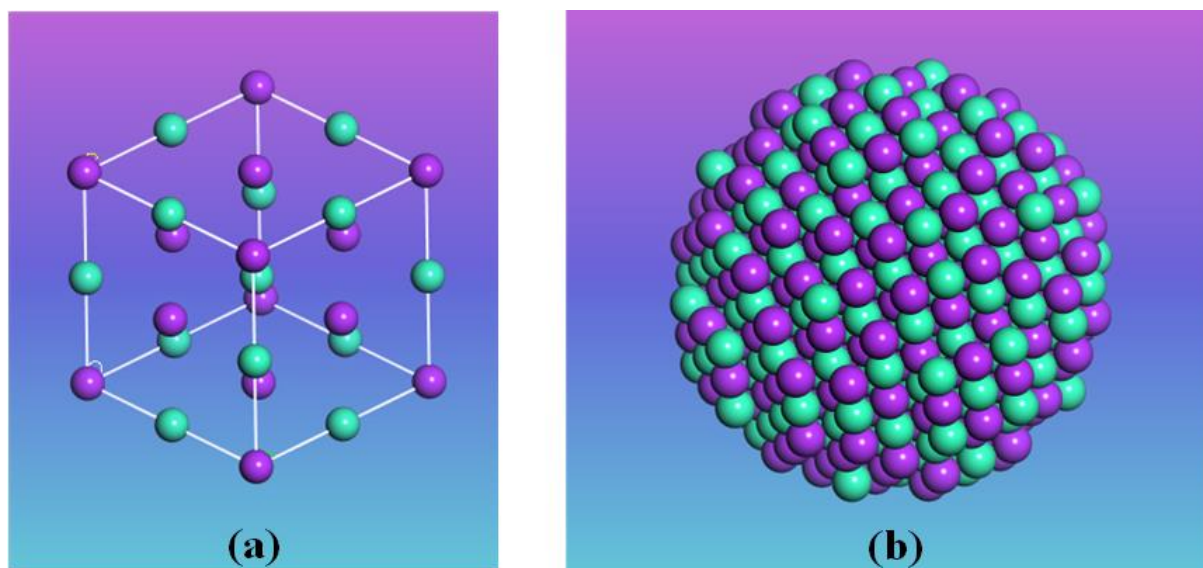
The parameters of Born-Mayer-Huggins potential are provided in **Table 1**.

**Table 1.** Born-Mayer-Huggins potential parameters for NaCl [12]

	$A_{ij}$ , kcal mol <sup>-1</sup>	$\sigma_{ij}$ , Å	$C_{ij}$ , kcal mol <sup>-1</sup> Å <sup>6</sup>	$D_{ij}$ , kcal mol <sup>-1</sup> Å <sup>8</sup>
Na-Na	6.0848	2.34	24.196	11.522
Na-Cl	4.8676	2.755	161.301	200.187
Cl-Cl	3.6509	3.17	1670.622	3355.646

## 2.2 Nanoparticle configuration

Before performing the MD simulation, nanoparticles with different sizes were built. Firstly, the crystal structure of chloride salts was generated, as **Figure 1a** shows. Then, this structure was integrated into spherical nanoparticles (Figure 1b). The diameter of nanoparticles ranges from 2.0 nm to 9.0 nm and the maximum ion number is 17072. The details of nanoparticle configuration are listed in **Table 2**. Finally, the produced nanoparticles were subjected to the cvff force field to optimize the structure [21]. The optimized nanoparticles were used as the initial configuration of MD simulation.

**Figure 1.** (a) Cubic crystal structure of NaCl and (b) NaCl nanoparticle (diameter = 3 nm). Na<sup>+</sup> and Cl<sup>-</sup> are colored purple and green respectively.

**Table 2.** Nanoparticle configuration

No.	Number of ion pairs	Total number of ions	Diameter, nm
#1	87	174	2.0
#2	298	596	3.0
#3	752	1504	4.0
#4	1473	2946	5.0
#5	4061	8122	7.0
#6	8536	17072	9.0

### 2.3 Simulation details

All the simulations were performed using the open-source MD simulation software LAMMPS. The Born-Mayer-Huggins and Coulombic interactions were truncated at 20 Å and the long-range corrections were applied [22]. The long-range Coulombic interactions were handled using the particle-particle-particle-mesh (pppm) method, meaning that interactions within the cutoff were computed directly while those outside the distance were calculated in reciprocal space. Verlet algorithm was employed to solve Newton’s motion equations with a time step of 1 fs [23].

In all the simulations, we adopted the “multi constant temperature” method rather than the “gradually heating and cooling” method so that the system can be equilibrated at each specific temperature for a long enough time [14]. Each simulated system was first subjected to a process of energy minimization. Subsequently it was equilibrated for 1000 ps at the desired pressure and temperature in the isothermal-isobaric (NPT) ensemble [24]. The pressure was fixed at 0.1 MPa while the temperature ranged from 400 K to 1200 K to cover both the solid and liquid state. During the simulation process, Nose-Hoover thermostat and barostat were employed to control the pressure and temperature. The damping parameters which determine how rapidly the temperature and pressure were relaxed are set as 100 fs and 500 fs, respectively.

### 3. Results and discussions

#### 3.1 Simulation of bulk salt

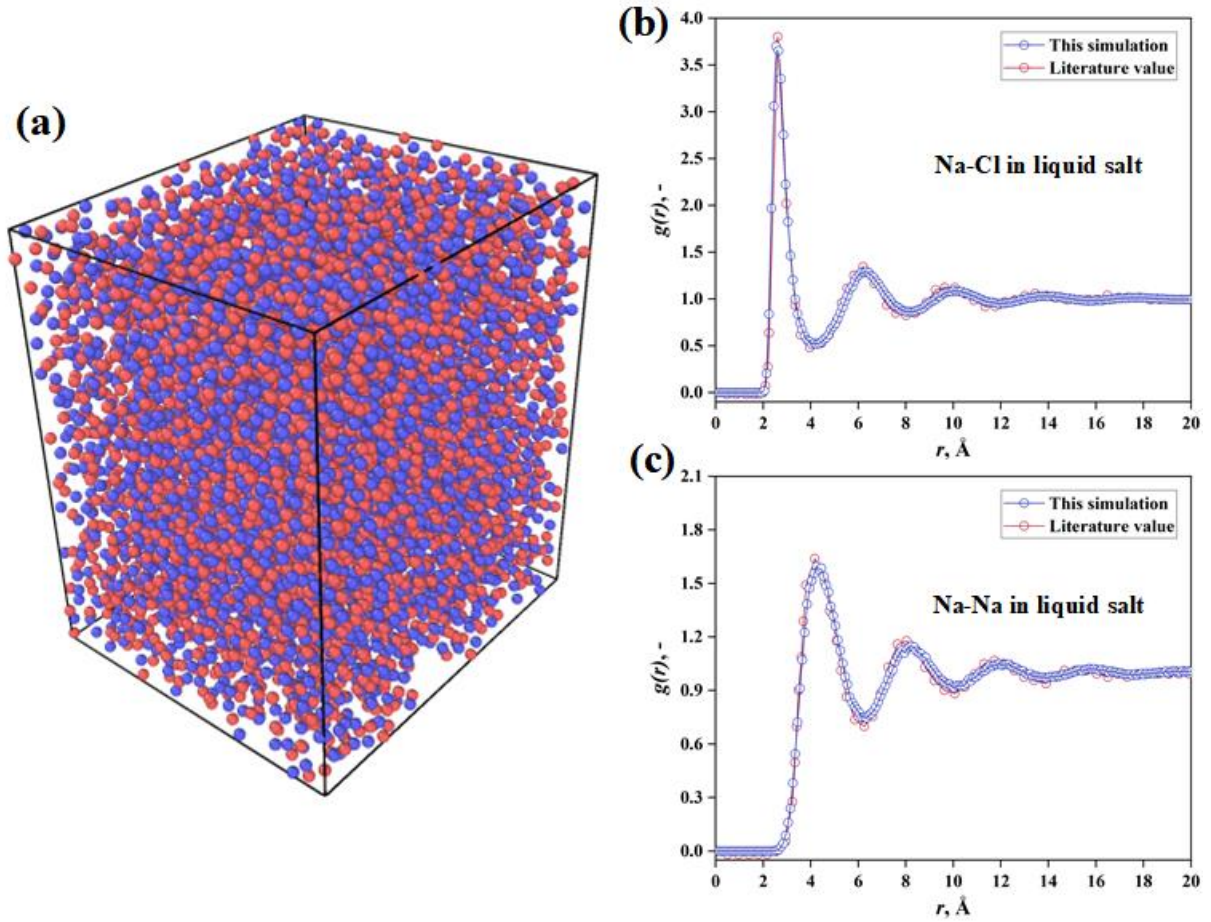


**Figure 2.** (a) Schematic of bulk NaCl system, red and blue spheres represent  $\text{Na}^+$  and  $\text{Cl}^-$ . (b)~(c) Comparison of simulated RDFs with literature values [12]: (b): Na-Cl, (c): Na-Na.

The bulk NaCl was also simulated and the system consists of 8192 atoms [23]. The schematic of the bulk NaCl system is shown in **Figure 2**(a). The system was first heated at 2000 K and then cooled to the desired temperature within 2ns [12]. Next, it was equilibrated in NPT ensemble for 1ns. The other simulation setup is the same as that mentioned in Section 2.3. The radial distribution function (RDF) describes the local structure of materials [25]:

$$g_{\alpha\beta}(r) = \frac{1}{4\pi\rho_{\beta}r^2} \left[ \frac{dN_{\alpha\beta}(r)}{dr} \right] \quad (4)$$

where  $\alpha$  and  $\beta$  denote  $\alpha$ -type ion and  $\beta$ -type ion, respectively;  $\rho_{\beta}$  is the number density of  $\beta$ -type ion;  $N_{\alpha\beta}(r)$  is the mean number of  $\beta$ -type ions lying in a sphere of radius  $r$  centred on an  $\alpha$ -type ion.

RDFs of Na-Na and Na-Cl in the liquid salt are presented in Figure 2(b)-(c). The RDFs were compared with the literature value [12] and it showed good agreement, which validates the accuracy of the model used in this study.

### 3.2 Melting behaviour

Lindemann index characterises the atomic motion by measuring the distance between atoms. The expression of Lindemann index of an individual atom is given by [26]:

$$\delta_i = \frac{1}{N-1} \sum_{j \neq i} \frac{\sqrt{\langle R_{ij}^2 \rangle - \langle R_{ij} \rangle^2}}{\langle R_{ij} \rangle} \quad (5)$$

where  $\delta_i$  is the Lindemann index of atom  $i$ ;  $N$  is the total ion number;  $R_{ij}$  is the distance between ion  $i$  and ion  $j$ ; the bracket denotes the ensemble average. Lindemann index distributions (LIDs) of 4nm nanoparticle are presented in **Figure 3**. At 700 K, the Lindemann index of most atoms is small because the atomic motion is restricted by the crystal lattice and atoms vibrate “in place” [27], indicating NaCl at the solid state. When the temperature increases to 900 K, the atomic motion increases and the Lindemann index becomes larger. However, the overall intensity of atomic motion is still weak. When the temperature rises to 1000 K, the Lindemann index of all atoms is obviously large. Atomic motion is free and not restricted, indicating the destruction of the crystal lattice and the transition from the solid to liquid.

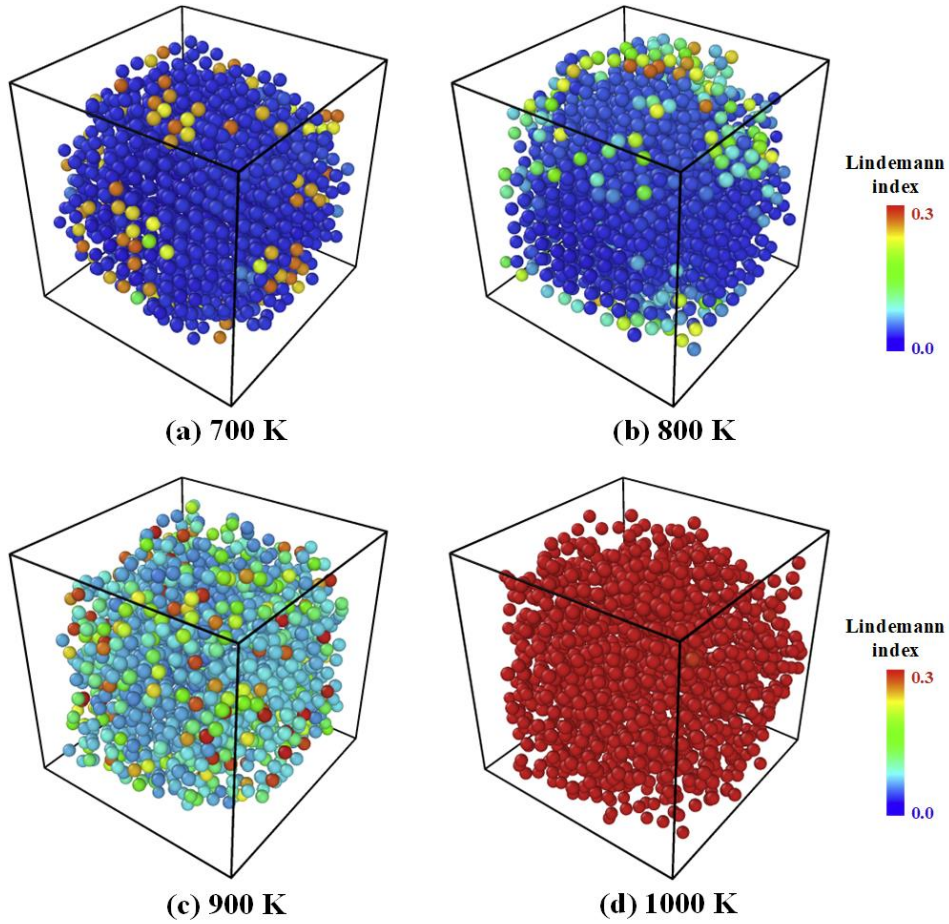


**Figure 3.** Lindemann index distribution of 4nm NaCl nanoparticle at different temperature

### 3.4 Melting point

Lindemann index method [28] and total energy method [15] are used in the current study to identify the melting point. The global Lindemann index is defined as the average value of Lindemann index of all individual atoms:

$$\delta = \frac{1}{N} \sum_i \delta_i \quad (6)$$

where  $N$  is the total ion number. The global Lindemann index characterizes atomic motion by measuring the distance between atoms. The Lindemann index method determines the temperature where the abrupt increase in the global Lindemann index ends as the melting point [28]. By contrast, the total energy method identifies the temperature where the total system energy jumps as the melting point [15].

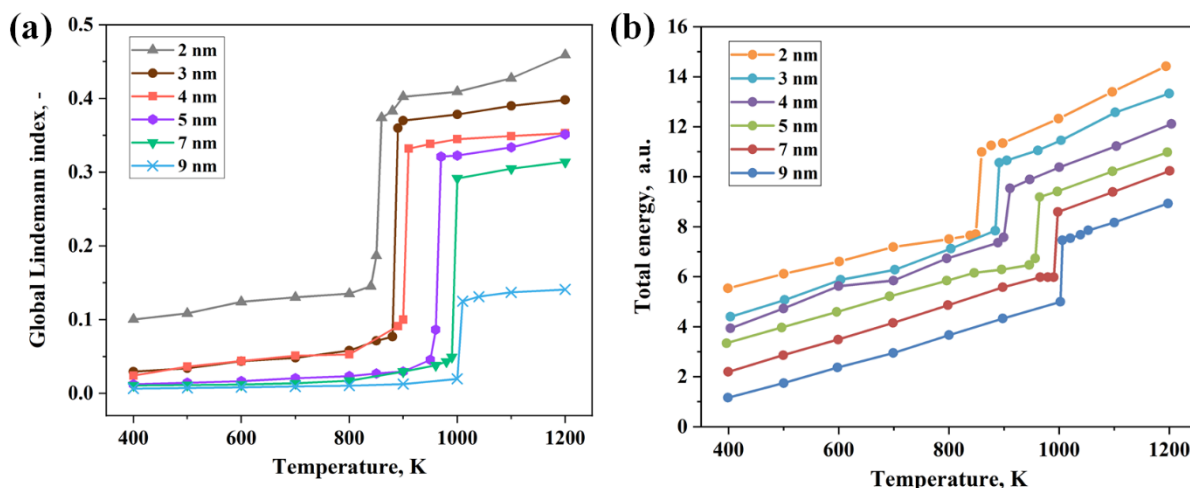


**Figure 4.** (a) Variation of global Lindemann index of different NaCl nanoparticles. (b) Variation of total energy with temperature.

The variation of global Lindemann index and total energy is shown in **Figure 4**. It is seen that both the global Lindemann index and total energy increases with the temperature and they jump at a certain temperature. The jumps is used to determine the melting point.

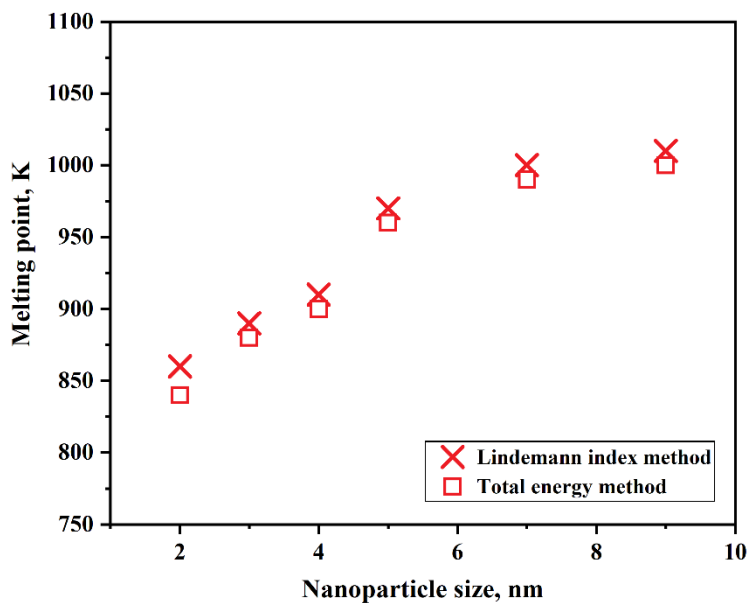


**Figure 5.** Melting point predicted by Lindemann index method and total energy method

**Figure 5** presents the melting point of different NaCl nanoparticles. The melting point decreases with the decreasing nanoparticle size, which is a common phenomenon for many materials [14, 16, 29]. It is noted that, as Figure 5 shows, the melting point predicted by the Lindemann index method is larger than those by the total energy method. It could be attributed

to the different definition of melting point in these two methods. For the Lindemann index method, the melting point is identified as the temperature where the abrupt increase of the global Lindemann index ends [28]. Atomic motion in the liquid PCM is obviously intensive than that in the solid PCM, so the global Lindemann index is larger significantly. The Lindemann index method considers the temperature where the abrupt increase of the global Lindemann index ends as the melting point. It identifies the lower limit of the liquid state. Regarding with the total energy method, the melting point is determined as the temperature where the total energy jumps [15]. When the solid PCM converts into liquid PCM, its total energy increases abruptly due to the latent heat. So, the total energy method identifies the upper limit of the solid state. Nevertheless, the Lindemann index method and total energy method describe the same melting process and the deviation in the melting point is reasonable. **The simulated melting point of bulk NaCl is 1050 K, as shown in Figure S1, agrees well with the experimental data [30].**

The comparison of LIDs of different NaCl nanoparticles is presented in **Figure 6**. It is obvious that at the same temperature, 2 nm nanoparticle has the largest Lindemann index, indicating that atoms in small nanoparticles vibrate more intensively. The relation of the global Lindemann index with the melting point is shown in Figure 6(d). It is seen that the larger the global Lindemann index, the lower the melting point. The variation of the melting point may be attributed to the relation of the destruction of the crystal lattice with the atomic vibration. Atoms vibrate more intensively in small nanoparticles. As the temperature increase, the vibration increases. For small nanoparticles, the vibration more easily reaches the critical value to destruct the crystal lattice. Thus, the melting point of small nanoparticles is low.

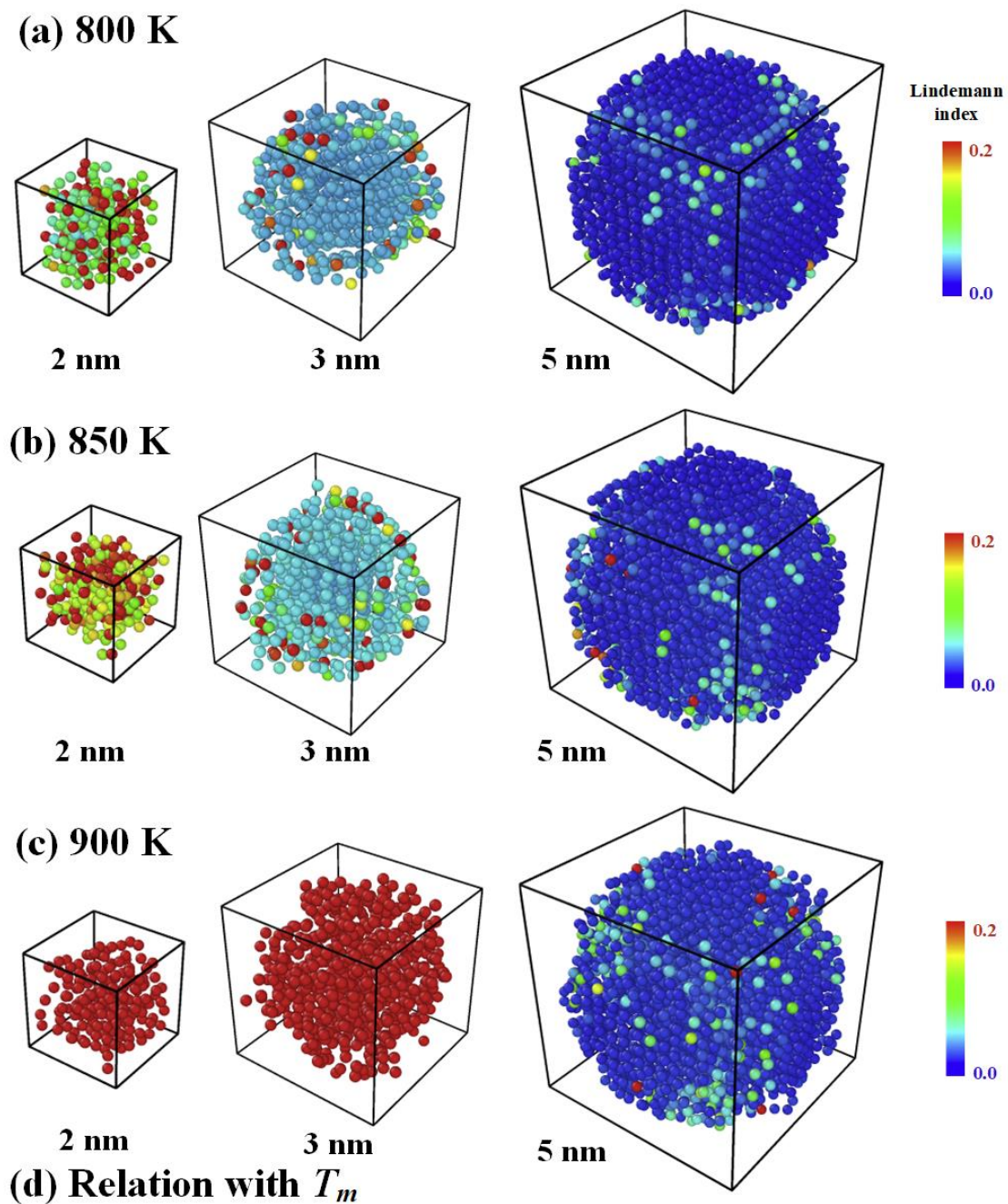


**Figure 6.** Comparison of Lindemann index distribution of NaCl nanoparticles with different sizes: (a) 800 K, (b) 850 K, (c) 900 K. (d) Relation of the global Lindemann index with melting point.

### 3.4 Latent heat

**Figure 7** shows the variation of enthalpy with temperature. At the solid state, the enthalpy increases with temperature. Near the melting point, it increases sharply due to the latent heat, followed by a stable rise.

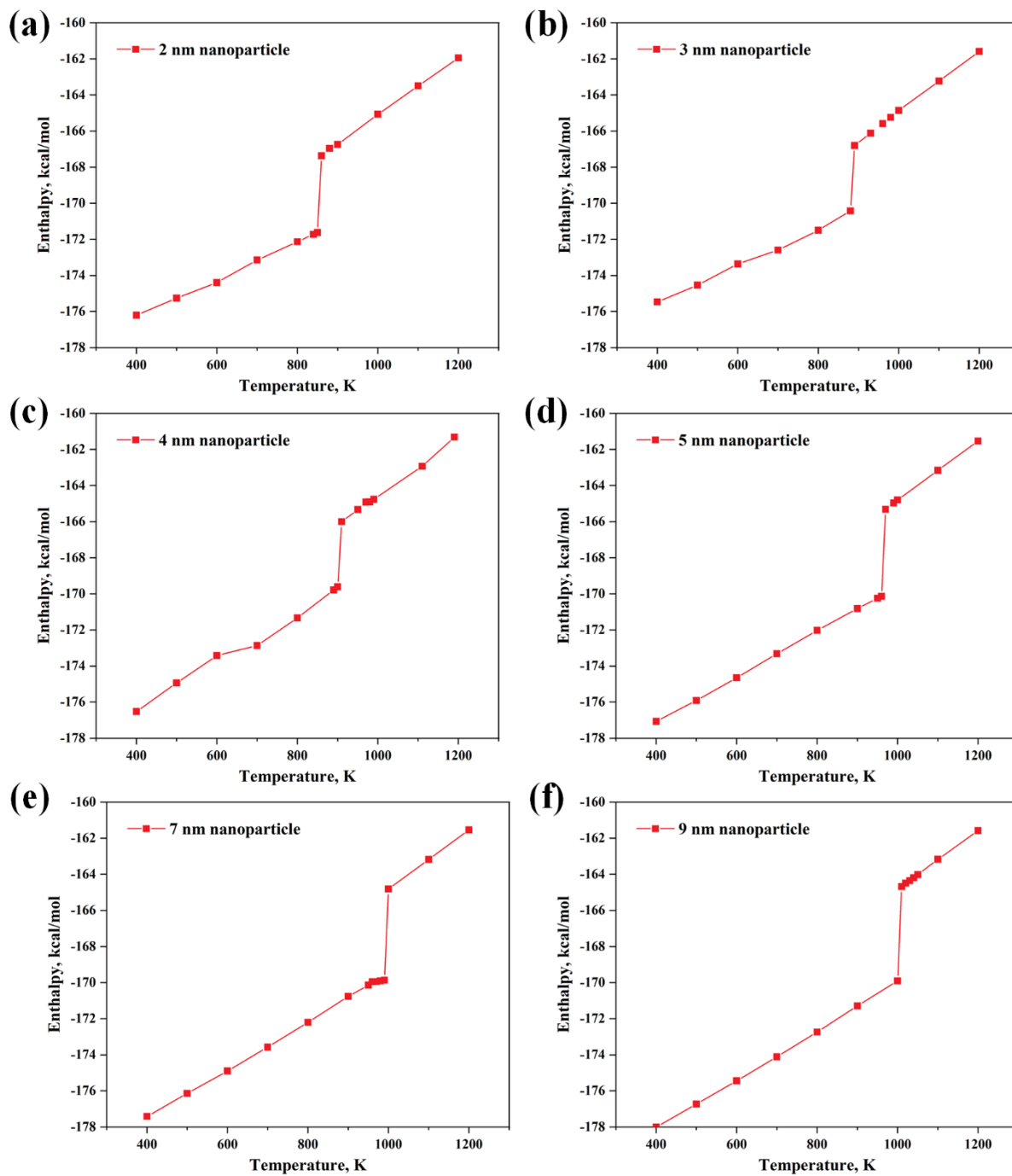


**Figure 7.** Variation of enthalpy with temperature: (a)–(f): 2 nm, 3 nm, 4 nm, 5 nm, 7 nm and 9 nm NaCl nanoparticle.

The latent heat is calculated based on the sharp increase in the system enthalpy [31]:

$$L = H_l - H_s \quad (7)$$

where  $H_l$  and  $H_s$  are the enthalpy of liquid NaCl and solid NaCl near the melting point.

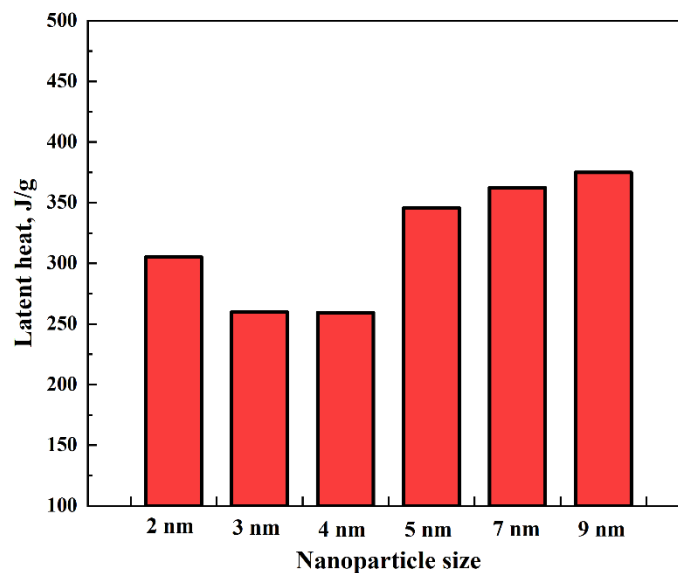


**Figure 8.** Latent heat of different NaCl nanoparticles.

The latent heat of different NaCl nanoparticles is shown in **Figure 8**. The result indicates that the 9nm nanoparticle has the maximum latent heat and the latent heat is 9 nm (375.0 J/g), 7 nm (362.3 J/g), 5 nm (345.6 J/g), 2nm (305.1 J/g), 3 nm (259.8 J/g) and 4 nm (259.2 J/g) in order from high to low. **The simulated latent heat of bulk NaCl is presented in Figure S1 and shows good agreement with experimental value.**

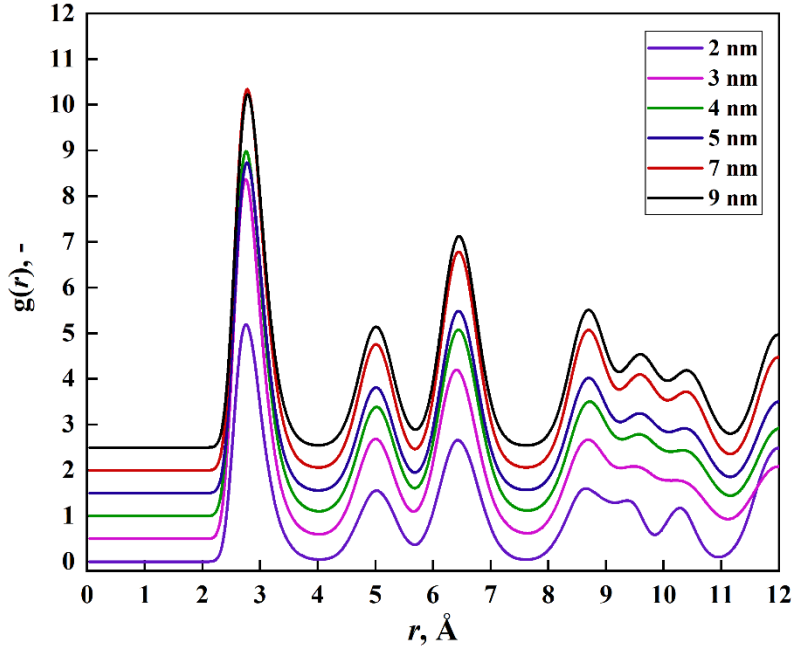


**Figure 9.** Radial distribution function of different NaCl nanoparticles at 600 K.

Latent heat is the energy required to destroy the crystalline lattice at the melting point [32].

The coordination number is the total number of atoms surrounding the central atom. It characterises the intensity of the close packing of atoms stacked in a crystal. The larger the coordination number, the tighter the atoms stack and the more stable the crystal structure [33].

The coordination number is calculated from the radial distribution function [25]:

$$N_{\alpha\beta} = 4\pi\rho_{\beta} \int_0^{r_{min}} g_{\alpha\beta}(r) r^2 dr \quad (8)$$

where  $r_{min}$  is the position of the first peak valley of RDF.

Radial distribution function curves of different NaCl nanoparticles are plotted in **Figure 9** and the first peak valley is located at 4.05 Å. Coordination number curves at 600 K are shown in **Figure 10**. It is seen that the coordination number is 9 nm (5.73), 7 nm (5.63), 5 nm (5.60), 2 nm (5.51), 3 nm (5.37) and 4 nm (5.36) in order from high to low, which is consistent with the latent heat. The smaller coordination number indicates the more loosely packed structure. Thus, less energy is required to destroy the crystalline lattice and the latent heat is decreased.

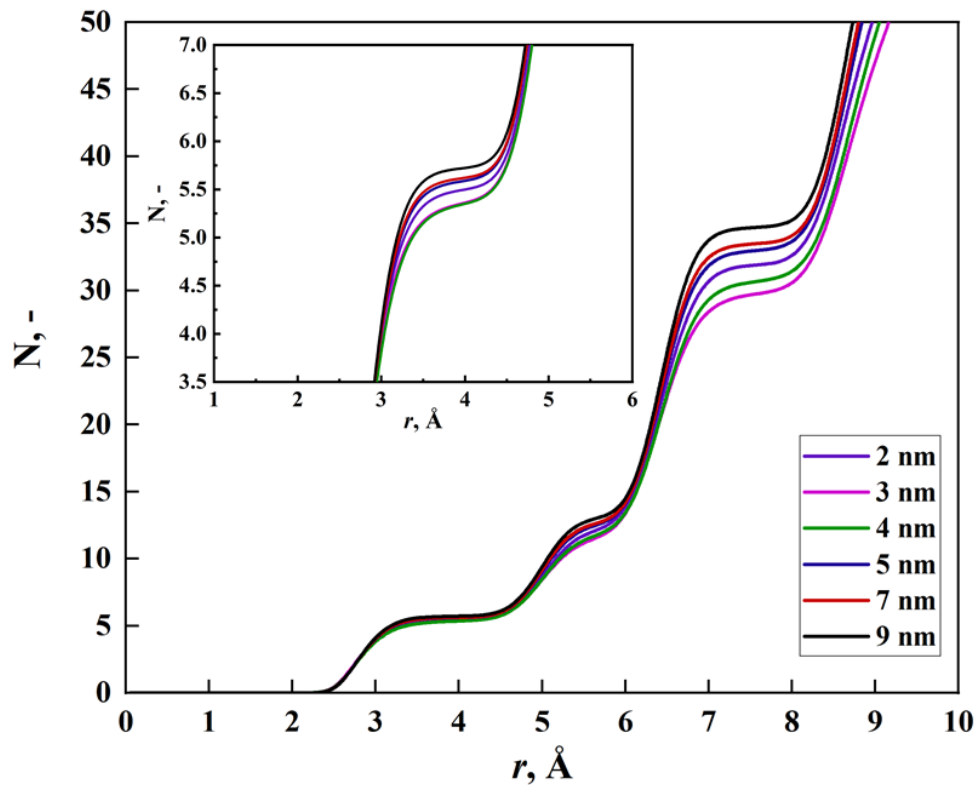


**Figure 10.** Coordination number curves of different NaCl nanoparticles at 600 K.

#### 4. Conclusions

In this paper, the underlying mechanism of the size effect on the melting point and latent heat of molten salt is revealed from the atomic point of view. NaCl was selected as the phase change material in the molecular dynamics simulation. It is found that the atomic motion in smaller nanoparticles is more intensive and thus the crystal structure of smaller nanoparticles is easier to be destroyed, which leads to a lower melting point. The order of the latent heat is consistent with that of the coordination number. The low coordination number means a loosely packed structure. As a result, less energy is required to destroy the crystalline lattice and the latent heat is decreased. Bulk molten salt was also simulated and the correctness of the simulation results was validated.

This paper provides microscopic insights into the depression of melting point and latent heat of nanoporous shape-stabilised phase change material. It is noted that as PCMs are embedded in nanopores, the depression of thermal properties may be due to the size effect,

interaction or both. Therefore, further study is needed to explore the depression of thermal properties of PCMs embedded in nanopores. In addition, the experimental work is very important to support the numerical results. However, it is of great difficulty to measure the melting point and latent heat of nanoscale molten salt due to the extreme high temperature and corrosion problem. A practical experiment is needed in the future research work.

## **Acknowledgements**

The authors would like to acknowledge the financial support by National Key R&D Program of China (No. 2018YFA0702300), H2020-MSCA-RISE-778104–ThermaSMART, Ningbo Science and Technology Bureau (No. 2019B10042), doctoral degree scholarship of China Scholarship Council (CSC). We are grateful for access to the University of Nottingham's Augusta HPC service.

## **Conflicts of interest**

There are no conflicts to declare.

## Nomenclature

PCM	Phase change material
ss-PCM	Shape-stabilized phase change material
TES	Thermal energy storage
MD	Molecular dynamics
LA	Lauric acid
LID	Lindemann index distribution
RDF	Radial distribution function
$T_m$	Melting point
$T_m^B, T_m^N$	Melting point of bulk material and nanoparticle
$\gamma_l, \gamma_s$	Surface tension
$\rho_s, \rho_l$	Density of solid and liquid material
$L$	Latent heat
$r$	Nanoparticle radius
$E_{i,j}$	Pairwise potential between atom $i$ and $j$
$r_{ij}$	Distance between two atoms
$A_{ij}, \sigma_{ij}, C_{ij}, D_{ij}$	Born-Mayer-Huggins potential parameters
$\rho$	Ionic-pair dependent length parameter
$E_{coul}$	Columbic interaction
$q_i, q_j$	Charge of ion $i$ and $j$
$\alpha, \beta$	$\alpha$ -type ion and $\beta$ -type ion
$\rho_\beta$	Number density of $\beta$ -type ion
$N_{\alpha\beta}(r)$	Mean number of $\beta$ -type ions lying in a sphere of radius $r$ centred on an $\alpha$ -type ion
$g_{\alpha\beta}$	Radial distribution function of $\alpha$ -type ion and $\beta$ -type ion

$\delta_i$	Lindemann index of atom $i$
$N$	Total atom number
$\delta$	Global Lindemann index
$T$	Temperature
$H_l, H_s$	Enthalpy of liquid and solid PCM

## References

- [1] E. Pomerantseva, F. Bonaccorso, X. Feng, Y. Cui, Y. Gogotsi, Energy storage: The future enabled by nanomaterials, *Science* 366 (6468) (2019) eaan8285, <https://doi.org/10.1126/science.aan8285>.
- [2] N. S. Lewis, Research opportunities to advance solar energy utilization, *Science* 351 (6271) (2016) aad1920, <https://doi.org/10.1126/science.aad1920>.
- [3] E. M. Shchukina, M. Graham, Z. Zheng, D. G. Shchukin, Nanoencapsulation of phase change materials for advanced thermal energy storage systems, *Chem. Soc. Rev.* 47 (11) (2018) 4156-4175, <https://doi.org/10.1039/C8CS00099A>.
- [4] S. Zhang, D. Feng, L. Shi, L. Wang, Y. Jin, L. Tian, Z. Li, G. Wang, L. Zhao, Y. Yan, A review of phase change heat transfer in shape-stabilized phase change materials (ss-PCMs) based on porous supports for thermal energy storage, *Renew. Sust. Energ. Rev.* 135 (2021) 110127, <https://doi.org/10.1016/j.rser.2020.110127>.
- [5] J. Tang, M. Yang, F. Yu, X. Chen, L. Tan, G. Wang, 1-Octadecanol@ hierarchical porous polymer composite as a novel shape-stability phase change material for latent heat thermal energy storage, *Appl. Energ.* 187 (2017) 514-522, <https://doi.org/10.1016/j.apenergy.2016.11.043>.
- [6] T. Nomura, C. Zhu, N. Sheng, K. Tabuchi, A. Sagara, T. Akiyama, Shape-stabilized phase change composite by impregnation of octadecane into mesoporous SiO<sub>2</sub>, *Sol. Energ. Mat. Sol. C.* 143 (2015) 424-429, <https://doi.org/10.1016/j.solmat.2015.07.028>.
- [7] R. A. Mitran, D. Berger, C. Munteanu, C. Matei, Evaluation of Different Mesoporous Silica Supports for Energy Storage in Shape-Stabilized Phase Change Materials with Dual Thermal Responses, *J. Phys. Chem. C.* 119 (27) (2015) 15177-15184, <https://doi.org/10.1021/acs.jpcc.5b02608>.

- [8] R.-A. Mitran, D. Lincu, L. Buhălțeanu, D. Berger, C. Matei, Shape-stabilized phase change materials using molten NaNO<sub>3</sub> – KNO<sub>3</sub> eutectic and mesoporous silica matrices, *Sol. Energ. Mat. Sol. C.* 215 (2020) 110644, <https://doi.org/10.1016/j.solmat.2020.110644>.
- [9] S. Liu, G. Ma, S. Xie, Y. Jia, J. Sun, Y. Jing, Diverting the phase transition behaviour of adipic acid via mesoporous silica confinement, *RSC Advances* 6 (113) (2016) 111787-111796, <https://doi.org/10.1039/C6RA23498D>.
- [10] K. B. Lee, S. M. Lee, J. Cheon, Size-Controlled Synthesis of Pd Nanowires Using a Mesoporous Silica Template via Chemical Vapor Infiltration, *Adv. Mater.* 13 (7) (2001) 517-520, [https://doi.org/10.1002/1521-4095\(200104\)13:7<517::AID-ADMA517>3.0.CO;2-8](https://doi.org/10.1002/1521-4095(200104)13:7<517::AID-ADMA517>3.0.CO;2-8).
- [11] X. W. Wang, G. T. Fei, K. Zheng, Z. Jin, L. De Zhang, Size-dependent melting behavior of Zn nanowire arrays, *Appl. Phys. Lett.* 88 (17) (2006) 173114, <https://doi.org/10.1063/1.2199469>.
- [12] G.-C. Pan, J. Ding, W. Wang, J. Lu, J. Li, X. Wei, Molecular simulations of the thermal and transport properties of alkali chloride salts for high-temperature thermal energy storage, *Int. J. Heat. Mass. Tran.* 103 (2016) 417-427, <https://doi.org/10.1016/j.ijheatmasstransfer.2016.07.042>.
- [13] G. Pan, X. Wei, C. Yu, Y. Lu, J. Li, J. Ding, W. Wang, J. Yan, Thermal performance of a binary carbonate molten eutectic salt for high-temperature energy storage applications, *Appl. Energ.* 262 (2020) 114418, <https://doi.org/10.1016/j.apenergy.2019.114418>.
- [14] D. Chen, T. S. Totton, J. W. J. Akroyd, S. Mosbach, M. Kraft, Size-dependent melting of polycyclic aromatic hydrocarbon nano-clusters: A molecular dynamics study, *Carbon* 67 (2014) 79-91, <https://doi.org/10.1016/j.carbon.2013.09.058>.
- [15] H. Loulijat, H. Zerradi, S. Mizani, E. m. Achhal, A. Dezairi, S. Ouaskit, The behavior of the thermal conductivity near the melting temperature of copper nanoparticle, *J. Mol. Liq.* 211 (2015) 695-704, <https://doi.org/10.1016/j.molliq.2015.07.074>.

- [16] W. X. Zhang, C. He, Melting of Cu nanowires: a study using molecular dynamics simulation, *J. Phys. Chem. C.* 114 (19) (2010) 8717-8720, <https://doi.org/10.1021/jp910246t>.
- [17] W. Xie, J. Ding, G. Pan, Q. Fu, X. Wei, J. Lu, W. Wang, Heat and mass transportation properties of binary chloride salt as a high-temperature heat storage and transfer media, *Sol. Energ. Mat. Sol. C.* 209 (2020) 110415, <https://doi.org/10.1016/j.solmat.2020.110415>.
- [18] B. Larsen, T. Førlund, K. Singer, A Monte Carlo calculation of thermodynamic properties for the liquid NaCl+KCl mixture, *Mol. Phys.* 26 (6) (1973) 1521-1532, <https://doi.org/10.1080/00268977300102671>.
- [19] J. E. Mayer, Dispersion and Polarizability and the van der Waals Potential in the Alkali Halides, *J. Chem. Phys.* 1 (4) (1933) 270-279, <https://doi.org/10.1063/1.1749283>.
- [20] F. Lantelme, P. Turq, Ionic dynamics in the LiCl–KCl system at liquid state, *J. Chem. Phys.* 77 (6) (1982) 3177-3187, <https://doi.org/10.1063/1.444192>.
- [21] T. Chakraborty, A. Hens, S. Kulashrestha, N. C. Murmu, P. Banerjee, Calculation of diffusion coefficient of long chain molecules using molecular dynamics, *Physica E* 69 (2015) 371-377, <https://doi.org/10.1016/j.physe.2015.01.008>.
- [22] S. Jayaraman, A. P. Thompson, O. A. von Lilienfeld, E. J. Maginn, Molecular simulation of the thermal and transport properties of three alkali nitrate salts, *Ind. Eng. Chem. Res.* 49 (2) (2010) 559-571, <https://doi.org/10.1021/ie9007216>.
- [23] J. Ding, G. Pan, L. Du, J. Lu, X. Wei, J. Li, W. Wang, J. Yan, Theoretical prediction of the local structures and transport properties of binary alkali chloride salts for concentrating solar power, *Nano Energy* 39 (2017) 380-389, <https://doi.org/10.1016/j.nanoen.2017.07.020>.
- [24] H. Ni, J. Wu, Z. Sun, G. Lu, J. Yu, Molecular simulation of the structure and physical properties of alkali nitrate salts for thermal energy storage, *Renew. Energ.* 136 (2019) 955-967, <https://doi.org/10.1016/j.renene.2019.01.044>.

- [25] J. Wang, Z. Sun, G. Lu, J. Yu, Molecular dynamics simulations of the local structures and transport coefficients of molten alkali chlorides, *J. Phys. Chem. B.* 118 (34) (2014) 10196-10206, <https://doi.org/10.1021/jp5050332>.
- [26] Y. Wen, H. Fang, Z. Zhu, S. Sun, A molecular dynamics study of shape transformation and melting of tetrahedral platinum nanoparticle, *Chem. Phys. Lett.* 471 (4-6) (2009) 295-299, <https://doi.org/10.1016/j.cplett.2009.02.062>.
- [27] R. P. Feynman, R. B. Leighton, M. Sands, *The Feynman Lecture on Physics*. Addison Wesley Longman: Massachusetts, 1963.
- [28] E. Goudeli, S. E. Pratsinis, Crystallinity dynamics of gold nanoparticles during sintering or coalescence, *AIChE J.* 62 (2) (2016) 589-598, <https://doi.org/10.1002/aic.15125>.
- [29] Y. Shibuta, T. Suzuki, Melting and nucleation of iron nanoparticles: A molecular dynamics study, *Chem. Phys. Lett.* 445 (4-6) (2007) 265-270, <https://doi.org/10.1016/j.cplett.2007.07.098>.
- [30] M. Liu, W. Saman, F. Bruno, Review on storage materials and thermal performance enhancement techniques for high temperature phase change thermal storage systems, *Renew. Sust. Energ. Rev.* 16 (4) (2012) 2118-2132, <https://doi.org/10.1016/j.rser.2012.01.020>.
- [31] L. Miao, V. R. Bhethanabotla, B. Joseph, Melting of Pd clusters and nanowires: a comparison study using molecular dynamics simulation, *Phys. Rev. B.* 72 (13) (2005) 134109, <https://doi.org/10.1103/PhysRevB.72.134109>.
- [32] M. Schmidt, R. Kusche, W. Kronmüller, B. von Issendorff, H. Haberland, Experimental determination of the melting point and heat capacity for a free cluster of 139 sodium atoms, *Phys. Rev. Lett.* 79 (1) (1997) 99, <https://doi.org/10.1103/PhysRevLett.79.99>.
- [33] G. L. Miessler, P. J. Fischer, D. A. Tarr, *Inorganic chemistry*. 5th edition; NJ: Pearson Prentice Hall: Upper Saddle River, 2014.